The High-Speed Deformation Behavior of High-Strength Lightweight Al-Li Alloy Sheets

Ali Abd El-Aty, Shi-Hong Zhang, Xunzhong Guo, Yong Xu, Ma Yan, Dayoung Chen, and Jie Tao

Abstract Since high-strength lightweight Al-Li alloys gained much attention recently, investigating the dynamic behavior of high-strength lightweight AA2060-T8 sheets is crucial because of their outstanding mechanical properties. Thus, uniaxial tensile tests were performed under high strain rate conditions using universal testing machines and split Hopkinson tensile bars. The ductility of AA2060-T8 sheets was improved under HSR deformation because of the adiabatic softening with increasing strain rate and the inertia effect, which may diffuse necking, slow down the necking development, and delay the onset of fracture. The present study results can efficiently develop a new manufacturing route based on impact hydroforming technology (IHF) to manufacture sound thin-walled-complex shape components from high-strength lightweight Al-Li alloy sheets at room temperature.

Keywords Al-Li alloys · AA2060-T8 · High-speed deformation · Impact hydroforming

1 Introduction

In recent years, Al-Li alloys have acquired much attention for their weight and stiffness-critical structures used in aircraft, military, and aerospace because of their superior outstanding properties, such as low density and high specific strength, than

A. Abd El-Aty (✉) · X. Guo · J. Tao
College of Material Science and Technology, Nanjing University of Aeronautics and Astronautics, Nanjing 211100, P.R. China

X. Guo · J. Tao
Jiangsu Key Laboratory of Nuclear Energy Equipment Materials Engineering, Nanjing University of Aeronautics and Astronautics, Nanjing 211100, P.R. China

A. Abd El-Aty · S.-H. Zhang · Y. Xu · M. Yan · D. Chen
Institute of Metal Research, Chinese Academy of Sciences, Shenyang 110016, P. R. China

A. Abd El-Aty
Mechanical Engineering Department, Faculty of Engineering-Helwan, Helwan University, Cairo, Egypt

G. Daehn et al. (eds.), *Forming the Future*, The Minerals, Metals & Materials Series,
https://doi.org/10.1007/978-3-030-75381-8_102

those of commercial Al alloys. The exceptional properties of Al-Li alloys are principally attributed to the added Li, which impacts the elastic modulus and weight reduction, where 1 wt.% of Li increases the elastic modulus by approximately 6% and reduces the resultant Al alloy's density by approximately 3% [1–3]. Based on the production date, Al-Li alloys are classified into three generations: first-generation Al-Li alloys such as AA1420, AA1421; second-generation Al-Li alloys such as AA8090, AA2090; and third-generation Al-Li alloys such as AA2050, AA2060 [2, 3].

AA2060-T8 is one of the newest candidates in the family of the third-generation Al-Li alloys launched by Alcoa Inc. in 2011 to replace AA2024-T3 and AA7075-T6 for upper and lower wings and fuselage structures [1, 3, 4]. The challenges associated with using AA2060-T8 sheets with conventional forming technologies are (1) poor formability because of the micro-voids and micro-cracks during processing; (2) anisotropic tensile properties, which caused serious issues during press forming; (3) and wrinkling and springback, which, in turn, adds to the cost of the die and the final products because of the try-out time. The aforementioned issues of AA2060-T8 restrict its broad applications [2, 3].

For the reason that AA2060-T8 was launched a few years ago, few studies on understanding the mechanical behavior, deformation mechanism, and anisotropic response of this alloy, notably at elevated temperatures, have been accomplished. For instance, Abd El-Aty et al. [5] studied the mechanical behavior and the texture evolution of AA2060-T8 during the bending process using PRM. Abd El-Aty et al. [6] learned the dislocation boundary structures of AA2060-T8 during the bending process, and they found that three types of microstructures were formed during bending. Ou et al. [7] revealed the deformation behavior of AA2060-T8 under hot forming conditions. Gao et al. [8] used their outstanding results [7] to investigate the feasibility of manufacturing aircraft components from AA2060-T8 using the HFQ process. Abd El-Aty et al. [4–6] proposed a computational method-based crystal plasticity modeling to link the mechanical response of AA2060-T8 sheets with their microstructural states and predict their deformation behavior at room temperature and different strain rates. Later, Abd El-Aty et al. [3] investigated the mechanical behavior of AA2060-T8 sheets at room temperature and a wide range of strain rates.

From the discussion mentioned above, it is evident that the quasi-static and high-speed deformation behavior of high-strength lightweight AA2060-T8 Al-Li alloy sheets and the constitutive relations which describe the flow behavior of AA2060-T8 sheets under high strain rate conditions are not investigated. The flow behavior of Al-Li and Al alloys under high strain rate deformation is complicated because they depend on several factors, such as the deformation mode, strain, and strain rates [9]. These factors control the strain hardening and dynamic softening, which affects the flow behavior and formability of these alloys [10–12]. Thus, characterizing the quasi-static and high-speed deformation behavior of high-strength lightweight AA2060-T8 Al-Li alloy sheets is meaningful to describe their mechanical response at various deformation conditions.

2 Experimental Procedures

The material used in this study was rolled AA2060-T8 sheet. HSR tensile tests were done using SHTB apparatus at room temperature to investigate the dynamic behavior of AA2060-T8 sheet at RD and strain rates of 1733, 3098, 3651, and 3919 s^{-1}. The sample orientations in HSR tensile tests were not considered since the sample orientations significantly impacted the case of quasi-static strain rates rather than HSR [1, 3]. The experimental setup of the SHTB apparatus and the details of the tensile specimen used in this test are depicted in Fig. 1. The HSR experiment was supposed to be started once the tensile sample was placed between the incident and the transmitter bars. However, the material being studied was rolled sheets with 2 mm thickness. Thus, a novel gripping method (clamp) was designed to integrate it in the SHTB apparatus for providing adequate clamping forces to avoid the tensile specimens from slipping during the experiments and introducing a low mechanical impedance to prevent the distortion of the waves. Once the novel clamp was implemented in the SHTB apparatus, the tensile specimen was placed between the incident and transmitted bars; thereafter, the striker situated on the incident bar impacted the flange, leading to the generation of a tensile wave (incident wave) that propagated along the incident bar, as depicted in Fig. 2. The strain gauge located on the incident bar recorded the incident wave ($\boldsymbol{\varepsilon_I}$) once it passed. Once the incident wave ($\boldsymbol{\varepsilon_I}$) hits the specimen, it is partly reflected ($\boldsymbol{\varepsilon_R}$) through the incident bar and partly transmitted ($\boldsymbol{\varepsilon_T}$) through the tensile specimen and the transmitted bar, as shown in Fig. 2. These reflected and transmitted waves were recorded by the strain gauges (using a high-velocity acquisition system, i.e., an oscilloscope) situated on the incident and transmitted bars, respectively. A schematic and a real set of waves detected during the SHTB experiment are depicted in Figs. 3 and 4. The progress of the HSR tensile

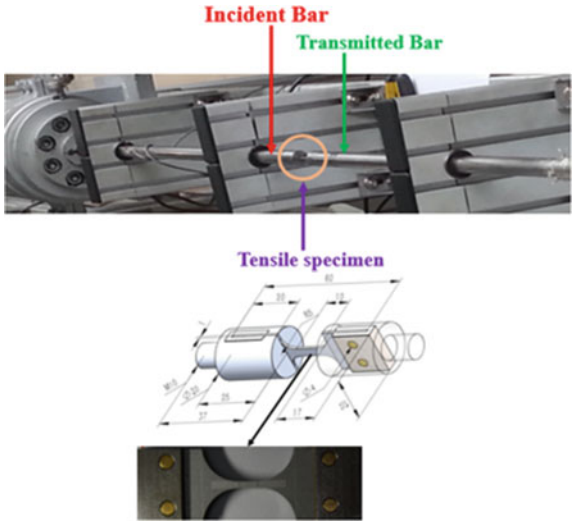

Fig. 1 The actual setup of the SHTB apparatus. (Color figure online)

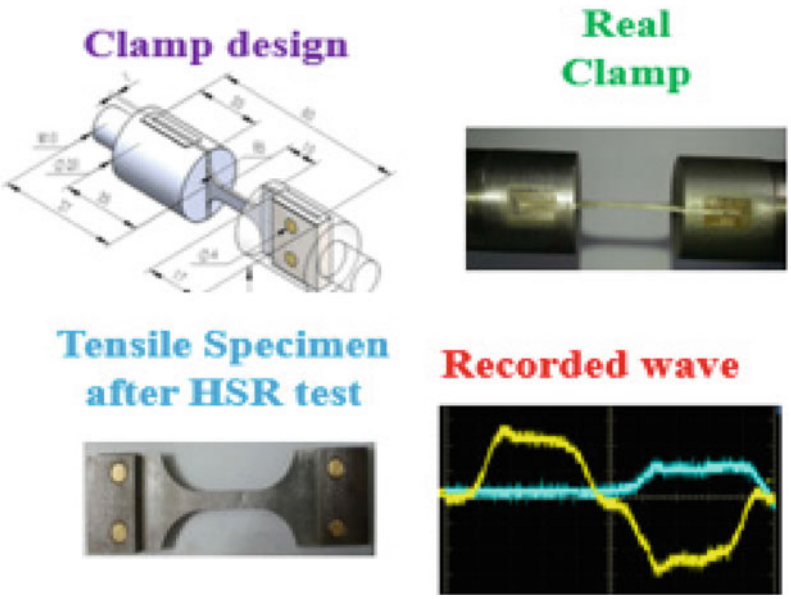

Fig. 2 The final version of the novel clamp used to avert the specimens from slipping during the test. (Color figure online)

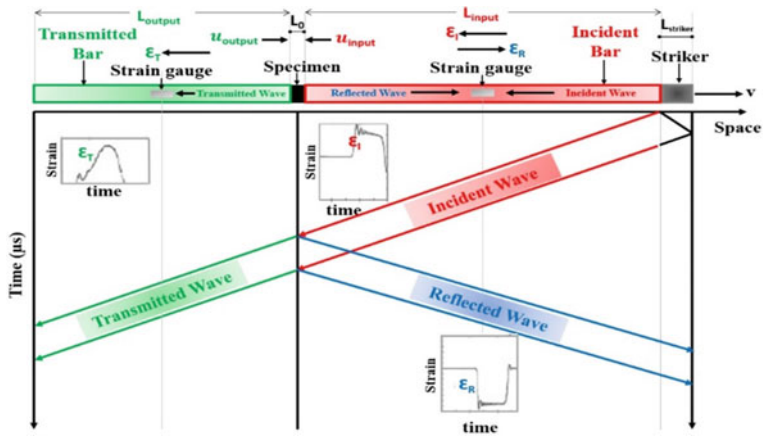

Fig. 3 The schematic representation of stress waves propagation in the bars. (Color figure online)

specimen during HSR tensile testing is illustrated in Fig. 5.

For simplicity, it was assumed that the equilibrium condition was verified during all the test, thus the mean strain and mean stress are generalized as:

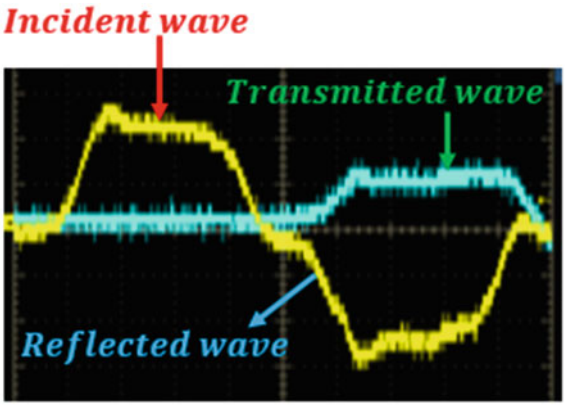

Fig. 4 The waveforms recorded by the oscilloscope during the HSR test. (Color figure online)

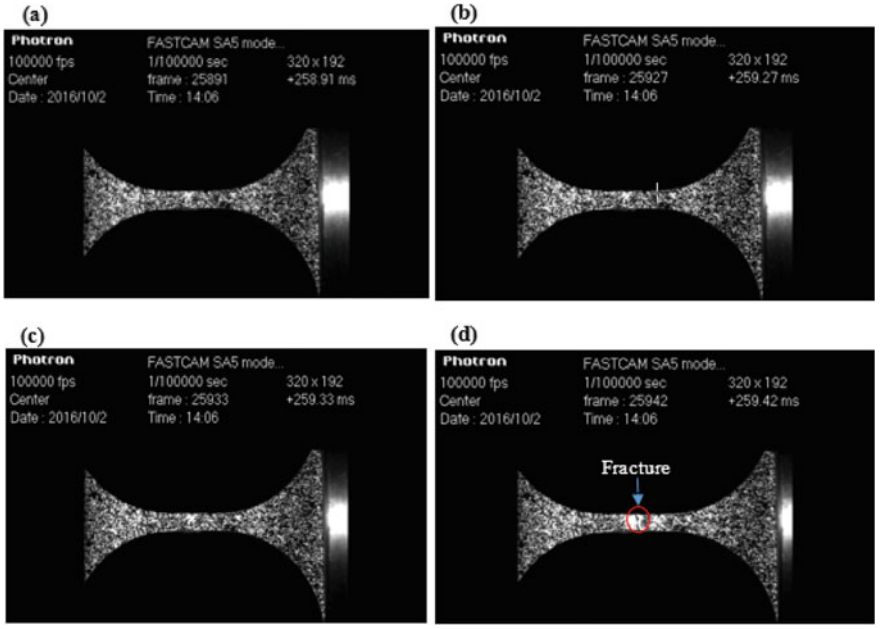

Fig. 5 The HSR tensile specimen **a** at the beginning of HSR tensile testing; **b** after 36 μs; **c** after 41 μs; and **d** after 51 μs from the beginning of HSR testing, in which the tensile specimen was broken. (Color figure online)

$$\varepsilon(t) = -\frac{2C}{L_0}\int_0^t \varepsilon_R(t)dt \tag{1}$$

$$\sigma(t) = E\frac{A}{A_0}\varepsilon_T(t) \tag{2}$$

The promptly axial strain rate ($\dot{\varepsilon}$) in the tensile sample was calculated from the first derivative of Eq. 1, so it can be written as

$$\dot{\varepsilon}(t) = \frac{v_{\text{input}}(t) - v_{\text{output}}(t)}{L_0} = -\frac{2C}{L_0}\varepsilon_R(t) \tag{3}$$

From Eq. 3, it could be perceived that with the SHPB equipment, the tests are not performed precisely at a constant strain rate. Only in the ideal case of the perfectly rectangular reflected wave, i.e., an entirely plastic response of the specimen, the strain rate is constant during the whole specimen deformation. In practice, this is almost impossible to observe and, generally, the nominal strain rate (average value of the effective strain rate) which used to indicate the strain rate of tests performed on the Hopkinson bar apparatus. Thus the HSR experiments were accomplished at strain rates of 1733, 3098, 3651, and 3919 s^{-1}.

3 Results and Discussion

3.1 Stress–Strain Behavior

The (σ_e, e) curves of AA2060-T8 sheets under HSR conditions are shown in Fig. 6. The work hardening behavior observed in HSR testing is more prominent than that

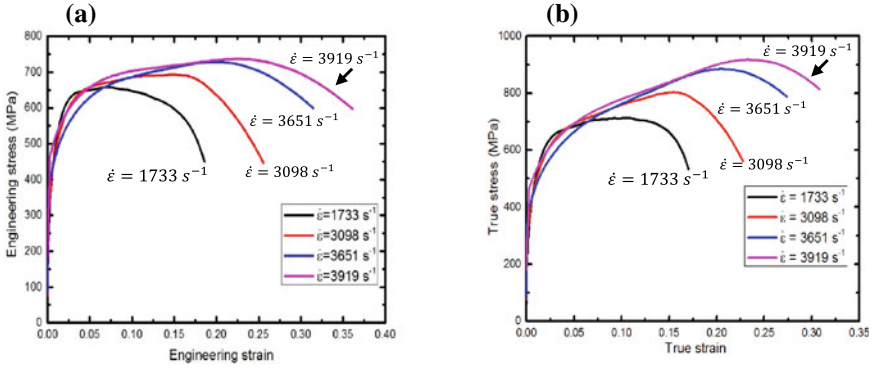

Fig. 6 **a** Engineering, and **b** true stress–strain curves of AA2060-T8 sheets at RD and HSR zone (i.e., $\dot{\varepsilon} = 1733s^{-1}$,$\dot{\varepsilon} = 3098s^{-1}$, $\dot{\varepsilon} = 3651s^{-1}$, and $\dot{\varepsilon} = 3919s^{-1}$). (Color figure online)

detected in QSR and ISR testing [1–3]. Thus, the yield, flow, and ultimate tensile stresses at HSR were higher than their QSR and ISR counterparts, which are generally attributed to the increased strain rates. Notwithstanding, the strain hardening rate observed in HSR testing was lower than that in QSR and ISR testing. This is attributed to the competition between the strain hardening and thermal softening due to adiabatic temperature rise with increasing strain rate. Thus, adiabatic softening influence is significant in HSR deformation and leads to abnormal mechanical behavior [34–37]. The strain rate increased to 1733, 3098, 3651, and 3919 s^{-1} (i.e., strain rate changed from QSR to HSR). The elongation to fracture of AA2060-T8 sheets in the HSR zone was simultaneously improved by increasing the strain rate, which is an appealing feature in HSR deformation. This enhancement is attributed to the adiabatic softening with increasing the strain rate and the inertia effect, which may diffuse necking, slow down the necking development, and delay fracture onset.

3.2 Design and Manufacturing a Novel Machine Based on IHF Technology

Based on the results mentioned above and the results obtained from Ma et al. [13], a new manufacturing route based on HSF was developed and denoted as IHF. Based on this new manufacturing route and principle of IHF, an advanced IHF machine was designed and manufactured, depicted as Fig. 7. There are four zones in this machine. Power zone can provide very high acceleration to the projectile, which is as high as 3200 m/s^2. The acceleration zone supplies the acceleration distance for the projectile and the release rig. The dynamic resistance reduction technology is implemented by controlling the air and adopting a special structure to reach high impact velocity.

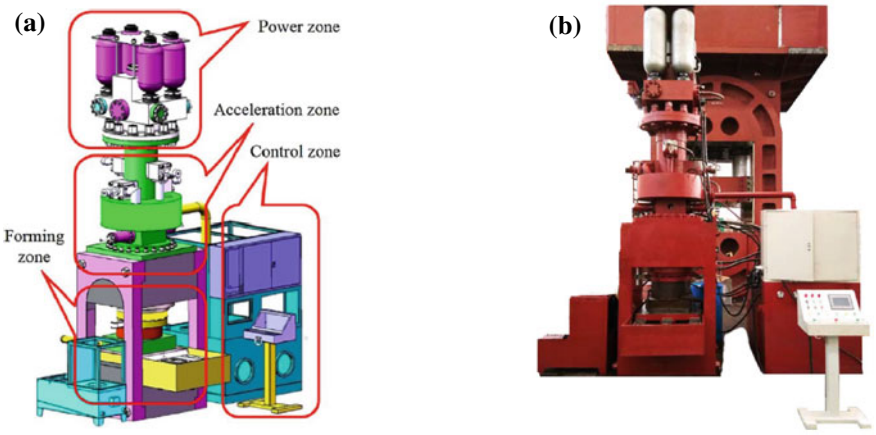

Fig. 7 (**a**) The schematic description, and (**b**) actual setup of IHF machine. (Color figure online)

Forming zone supplies the liquid chamber, binder hydraulic cylinder, and moveable working table. The control zone supplies the control function to all of the hydraulic valves to control the equipment's action. And the machine can run both under manual and automatic mode by inputting the code to the control board. The current research equipment's power source is the hydraulic-driven system, which can provide higher forming energy. For previous works, the power source is a pneumatic or explosive material, and their projectile is a solid cylinder that can freely move in the acceleration tube. The projectile of the current equipment is connected and controlled by a driven rod, capable of realizing more precise control. Furthermore, this equipment is more automatically run, which is suitable for industrial applications. The projectile's mass and the impact velocity and impact energy of the designed IHF machine are 60 kg (changeable), 10–80 m/s, and 3–200 kJ, respectively. The diameter and the volume of the liquid chamber are 250 mm (changeable) and 3–9 L. The dimensions of the working table are 800×800 mm, the max blank holder force is 250 T, and the binder hydraulic cylinder can be opened up to 400 mm.

3.3 Bulging Test

This novel IHF machine was used in this study to conduct a hydro-bulging test to investigate the formability of AA2060-T8 sheets under IHF loads and compare these results obtained from the bulging test under conventional hydroforming (quasi-static loading) loading. The specimens used in the bulging test were machined from AA2060-T8 sheets, and the radius of these samples is 83.6 mm.

Since the IHF machine's impact energy is 3–200 kJ, the impact velocity can be reached up to 80 m/s. As depicted in Fig. 7, the test specimen placed on the lower and upper dies was fixed on the master cylinder of the IHF machine by the fixing ring. The locating ring was used to guide the upper die to the right position along the axial direction. After the upper die contacted the test specimen with suitable clamping pressure, the high-speed hammer accelerated the liquid (Projectile). Thereafter, the test specimen was formed by the liquid with high energy in the shock wave. The velocity sensor was set in the chamber's lateral wall, whose position was near the liquid's upper surface to detect exactly the final velocity of the accelerated hammer. Each test condition was investigated at least three times to ensure consistency and repeatability.

The bulge height (h_B) of each test specimen was measured as depicted in Fig. 8 to assess the IHF loading effect on the formability of AA2060-T8 sheets and build up a window to describe the relationship between the impact energy (E_I) and the corresponding bulge height. This window is denoted as bulge height–impact energy (h_B–E_I) window, as presented in Fig. 9. The impact energy was used in this study instead of the pressure because the projectile's speed and mass mainly decide the impact energy. Furthermore, it is easy to calculate it compared to the pressure, especially under IHF conditions. As shown in the (h_B–E_I) window, under the IHF loading, the bulge heights of the test specimens were increased by increasing the impact energy

Fig. 8 The measurement tool used to measure the bulge height of each test specimen. (Color figure online)

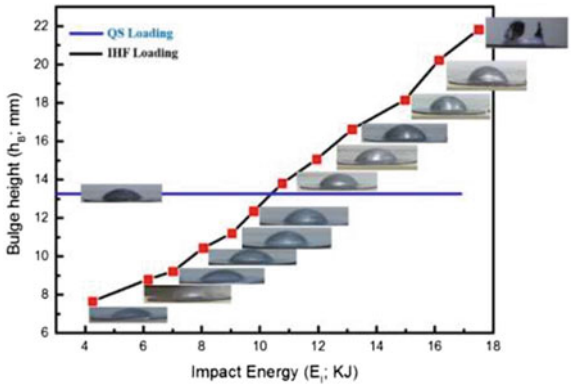

Fig. 9 Bulge height–impact energy (h_B–E_I) window describing the relation between the impact energy (k_J) and the corresponding bulge. (Color figure online)

up to 16.2 kJ; beyond this value, the test specimens were ruptured. The max bulge height obtained from IHF loading before rupture was 20.23 mm; however, the max bulge height obtained from conventional hydroforming loading using max pressure of 28 MPa was 13.3 mm as depicted in (h_B–E_I) window. This means and proves that the developed IHF technology can improve the formability of AA2060-T8 sheets at room temperature.

3.4 Manufacturing Aircraft Frame Part by IHF Technology

To investigate IHF technology's feasibility to fabricate thin-walled complex-shaped components, a complicated aircraft frame part was selected as a case study. The details of the aircraft frame part are depicted in Fig. 13. As shown in Fig. 13a, the aircraft frame part consists of eight convex shapes, outer surfaces, two concaves (concave 1 and concave 2), with drawing ratios (DR) of 3.88 and 3.52, respectively.

The ***DR*** in this study was calculated from Eq. 4 as:

$$DR = \frac{\textbf{blankarea}}{\textbf{concavearea}} \tag{4}$$

Because of the complexity of the shape of the aircraft frame and high ***DR*** compared to the common DR limit of steel sheets, 2 or many redrawing steps were required to reduce the DR for each step. The convex zones between the two concave zones are relatively easy to crack, as depicted in Fig. 10b since the strain is easy to exceed the forming limits. Furthermore, there are many small fillets (2 mm) at the outer surfaces and the concaves' bottoms. These small fillets increase the difficulties of forming this component. According to the theories of hydroforming, the smaller the radius, the higher the pressure, since it is challenging to supply the material to the radius zone because of the frictions under the high pressure, and form the material which already contacted the surface of the die and supply the material to the radius zone because of the friction under this increased pressure.

In the beginning, actual trials were performed to investigate the feasibility of forming the aircraft frame part using a quasi-static sheet hydroforming process (QS-SHF). As depicted in Fig. 11a, b large crack has appeared, and the outer surface of the frame part has a wrinkling tendency. This is because there is not enough material flowing to the fillet area to achieve the feeding effect. The rounded material's plastic deformation ability cannot meet the forming requirements, thus causing large area cracking. Therefore, the IHF technology was used to address the issues mentioned

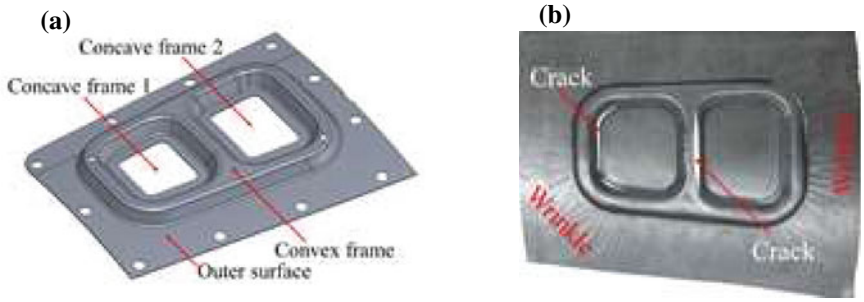

Fig. 10 **a** The aircraft frame part's details, **b** The actual aircraft frame part with wrinkle and crack formed by sheet hydroforming process (SHF). (Color figure online)

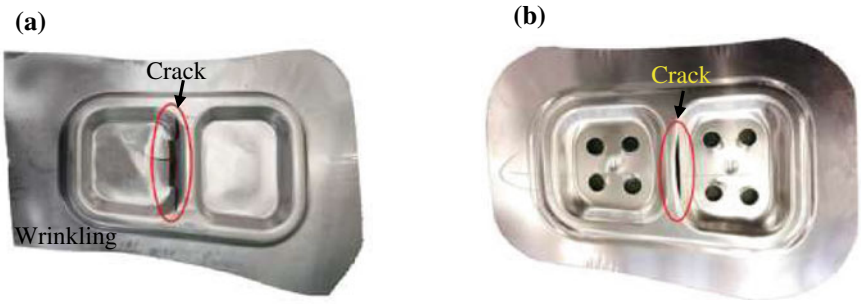

Fig. 11 Actual trials to produce the frame part by one step **a** QS-SHF, **b** IHF. (Color figure online)

above of QS-SHF. It is observed that the formability of the AA2060-T8 sheets was improved under the HSR condition. Furthermore, the cracking tendency and wrinkling were reduced compared to QS-SHF. However, the final product still has a small crack, as depicted in Fig. 11b. By analyzing the results obtained from both one-step QS-SHF and IHF, as shown in Fig. 11, it is challenging to manufacture the frame part by the one-step forming process. This is attributed to the high ***DR*** of concave 1 and concave 2. Thus, multi-step forming processes were used to overcome the limitations of the one-step forming process.

First, the pre-forming stage was accomplished using QS-SHF. The pre-forming stage improved and controlled the flow and the distribution of the material during the deformation. After that, to investigate and compare the effect of forming process on the formability and the crack tendency, the second forming stage was performed using either QS-SHF or IHF. Based on the original design of the frame part, the pre-formed parts were proposed as depicted in Fig. 12, since the rounded part of the inner side of the two cavities was increased from 2 to 20 mm. Furthermore, the width of the eight convex shapes is also increased.

After successfully carrying out the pre-forming stage, many trials were performed using both QS-SHF and IHF as a second forming stage. It is observed that the cracks still exist in the frame part produced by QS-SHF. However, no cracks were detected,

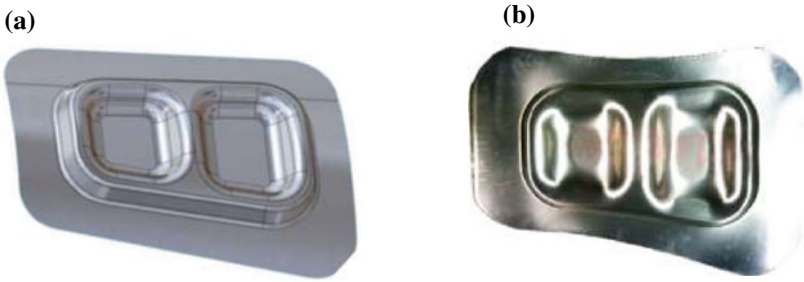

Fig. 12 **a** The CAD model, and **b** the actual trial of the pre-formed frame part. (Color figure online)

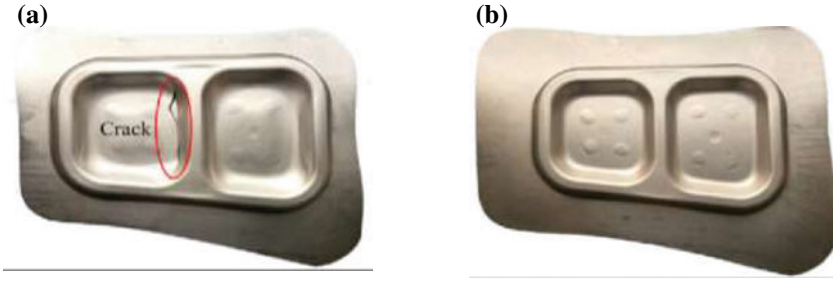

Fig. 13 The frame part was produced by **a** QS-SHF, **b** IHF after pre-forming. (Color figure online)

and the wrinkling was reduced in the frame part produced by IHF, as depicted in Fig. 13.

4 Conclusions

The main conclusions of this investigation can be deduced based on the achieved results as follows:

1. The work hardening behavior observed in HSR deformation is more prominent than that detected in QSR deformation. Thus, the YS, flow stress, and UTS at HSR were higher than their QSR counterparts. The strain hardening rate observed in HSR deformation was lower than that in QSR deformation, which was attributed to the competition between the strain hardening and thermal softening due to increasing the adiabatic temperature with increasing strain rate. The ductility of AA2060-T8 sheets was improved under HSR deformation because of the adiabatic softening with increasing strain rate and the inertia effect, which may diffuse necking, slow down the necking development, and delay the onset of fracture.
2. These results obtained from this study were efficiently used to develop a new manufacturing route called impact hydroforming technology (IHF). The IHF technology can improve the formability of lightweight metals and manufacture thin-walled complex-shaped components from Al-Li and Al alloys.

Acknowledgments The authors greatly acknowledge the financial support from the National Natural Science Foundation of China—International (Regional) Cooperation and Exchange Program (No. 5201101342), Jiangsu Province Science and Technology Project (No. BK20200453), and the National Natural Science Foundation of China (Grant No. 51875548).

References

1. Abd El-Aty A, Xu Y, Guo X, Zhang S, Ma Y, Chen D (2018) Strengthening mechanisms, deformation behavior, and anisotropic mechanical properties of Al-Li alloys: a review. J Adv Res 10:49–67
2. Rioja R, Liu J (2012) The evolution of Al-Li base products for aerospace and space applications. Metall Mater Trans A 43A:3325–3337
3. Abd El-Aty A, Xu Y, Zhang S, Ma Y, Chen D (2017) Experimental investigation of tensile properties and anisotropy of 1420, 8090 and 2060 Al-Li alloys sheet undergoing different strain rates and fibre orientation: a comparative study. Procedia Eng 207:13–18
4. Abd El-Aty A, Xu Y, Ha S, Zhang S (2018) Computational homogenization of tensile deformation behaviors of a third generation Al-Li alloy 2060–T8 using crystal plasticity finite element method. Mater Sci Eng A 731:583–594
5. Abd El-Aty A, Ha S, Zhang S, Xu Y (2018) Prediction of tensile deformation behavior of Al-Li alloy 2060–T8 by computational homogenization-based crystal plasticity finite element method. J Phys Conf Ser 1063:12058
6. Abd El-Aty A, Zhang S, Xu Y, Ha S, Deformation behavior and anisotropic response of 2060 Al-Cu-Li alloy: experimental investigation and computational homogenization-based crystal plasticity modelling. J Mater Res Technol
7. Ou L, Zheng Z, Nie Y, Jian H (2015) Hot deformation behavior of 2060 alloy. J Alloys Compd 648:681–689
8. Gao H, Weng T, Liu J, Li C, Li Z, Wang L (2016) Hot stamping of an Al-Li alloy: a feasibility study. Manufacturing Rev 9:9–15
9. Lin Y, Chen X (2011) A critical review of experimental results and constitutive descriptions for metals and alloys in hot working. Mater Des 32:1733–1759
10. Liang H, Nan Y, Ning Y, Li H, Zhang J, Shi Z, Guo H (2013) Correlation between strain-rate sensitivity and dynamic softening behavior during hot processing. J Alloy Compd 632(25):478–485
11. Babu B, Lindgren L (2013) Dislocation density based model for plastic deformation and globularization of Ti-6Al-4V. Int J Plast 50(8):94–108
12. Derogar A, Djavanroodi F (2011) Artificial neural network modeling of forming limit diagram. Mater Manuf Process 26(11):1415–1422
13. Ma Y, Xu Y, Zhang SH, Banabic D, Abd E-A, Chen D et al (2018) Investigation on formability enhancement of 5A06 aluminium sheet by impact hydroforming. CIRP Ann 67(1):281–284